Defect and Diffusion Forum Vol. 331 (2012) pp 53-73
Online available since 2012/Sep/19 at www.scientific.net

doi:10.4028/www.scientific.net/DDF.331.53

Low background digital coincidence spectrometer – a tool for investigation of positron annihilation in flight

J. Čížek[1a], M. Vlček[1], F. Lukáč[1], O. Melikhova[1], I. Procházka[1], W. Anwand[2], M. Butterling[2], A. Wagner[2], G. Brauer[2]

[1]Faculty of Mathematics and Physics, Charles University in Prague, V Holešovičkách 2, CZ-18000 Praha 8, Czech Republic

[2]Institut für Strahlenphysik, Helmholtz-Zentrum Dresden-Rossendorf, PO Box 510 119, D-01314 Dresden, Germany

[a]jakub.cizek@mff.cuni.cz (corresponding author)

Keywords: positron annihilation in flight, Doppler shift, digital spectrometer.

Abstract. A digital spectrometer for low background gamma ray spectroscopy equipped with two high purity Ge detectors and a 12-bit two channel digitizer was employed for the investigation of positron annihilation-in-flight. Measurements were performed for positrons emitted by ^{68}Ge/^{68}Ga and ^{22}Na radioisotopes and annihilated in Cu and Mg targets. The contribution of the two-quantum positron annihilation-in-flight was clearly resolved in coincidence two-dimensional gamma ray energy spectra. The contribution of positrons annihilated in flight has a hyperbolic shape described well by the relativistic theory.

Introduction

An energetic positron implanted into a solid loses most of its kinetic energy within ~ 0.1 ps in collisions with electrons [1] and reaches thermal equilibrium with the host material typically within a few ps [2]. For positron with energies below 2 MeV which were studied in this work the energy loss by collisions with electrons dominates over the energy loss by bremsstrahlung radiation. Most positrons are annihilated in the thermalized state. However, there is a small but non-zero probability that a positron is annihilated in flight, i.e. prior to its thermalization during the slowing down process. The study of positron annihilation-in-flight is interesting for several reasons: (i) it provides a very clean test of quantum electrodynamics (QED), (ii) investigation of annihilation-in-flight improves the knowledge about positron thermalization in matter and (iii) anomalies in the positron annihilation-in-flight cross-section may disclose the presence of new particles [3,4].

Two-quantum positron annihilation-in-flight (TQAF) has been observed in past by several authors. An attempt to determine the TQAF cross section for positrons with energies from ~ 1 to 200 MeV was performed in early works [5,6] using beta and gamma scintillation counters. Later the interest in TQAF was resuscitated due to the search for anomalies in the electron-positron scattering cross-section near the Z^0 mass [7,8] and the search for new particles [3,4].

The coincidence Doppler broadening (CDB) technique [9] is based on a precise measurement of the energies of two gamma rays emitted simultaneously in the process of positron annihilation using a coincidence apparatus equipped with two high purity germanium (HPGe) detectors. The energies of the two annihilation gamma rays differ due to Doppler shift caused by a non-zero momentum of the annihilating electron-positron pair in the laboratory frame. In TQAF events the positron momentum substantially exceeds the momentum of electron which leads to a large Doppler shift in the energy of annihilation gamma rays. Moreover, positrons with high kinetic energies annihilate with equal probability with all electrons in the target. This makes it possible to detect annihilations with deepest core electrons which cannot be observed in the case of annihilation of thermalized positrons [10,11].

Recently we developed a new digital CDB spectrometer [12] where pulses from HPGe detectors are sampled in real time by a two-channel 12-bit digitizer. The acquired waveforms are stored in a computer and analyzed off-line by software. Digital processing enables a detailed examination of

the shape of detector signals and waveforms with distorted shapes can be very efficiently eliminated. It has been demonstrated [12] that such a procedure leads to a strong suppression of background in a CDB spectrum. Since TQAF is very rare process low background is crucial for an accurate measurement of this phenomenon. In this work we studied TQAF of positrons with energy up to 1897 keV. It has been demonstrated that the digital CDB spectrometer is an excellent tool for investigation of TQAF process.

Experimental Details

Positron sources. In this work we report results obtained using two β^+ emitters (i) ^{22}Na (iThemba Labs, activity ≈ 1 MBq) which is the most common source in positron annihilation spectroscopy and (ii) ^{68}Ge/^{68}Ga (iThemba Labs, activity ≈ 0.6 MBq) positron generator. Positrons emitted by ^{22}Na (half life $T_{1/2}$ = 2.6 year) exhibit a continuous energy spectrum with the end-point-energy $T_{+,f}$ = 545 keV. One secondary photon with energy of 1274 keV is emitted per each positron due to de-excitation of the daughter ^{22}Ne nucleus. The ^{68}Ge radioisotope (half life $T_{1/2}$ = 271 day) decays to ^{68}Ga by electron capture. The daughter ^{68}Ga nucleus (half life $T_{1/2}$ = 68 min) subsequently decays to ^{68}Zn by β^+ decay (branching ratio 89%) or by electron capture (branching ratio 11%). The positrons emitted by ^{68}Ga exhibits continuous energy spectrum with the end point energy $T_{+,f}$ = 1897 keV. Hence, compared to ^{22}Na the ^{68}Ge/^{68}Ga positron generator emits positrons with higher kinetic energies. Moreover, contrary to ^{22}Na the probability for emission of a secondary photon (energy of 1078 keV) is very low for the ^{68}Ge/^{68}Ga positron generator and equals 0.039 per positron.

Targets. Positrons emitted by ^{22}Na and ^{68}Ge/^{68}Ga sources were annihilated in Cu and Mg targets. The total statistics accumulated in CDB spectra fell in the range 10^8 - 10^9.

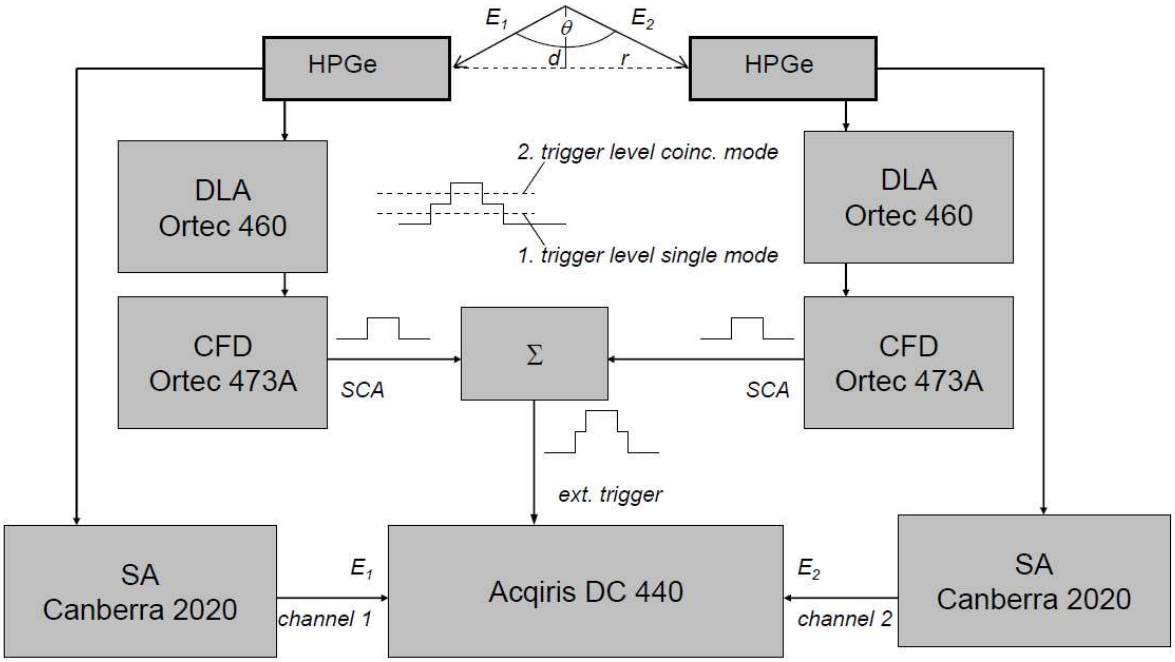

Figure 1 Scheme of digital CDB spectrometer used in this work. Meaning of the abbreviations in the figure: HPGe – high purity Ge detector, DLA – delay line amplifier, CFD – constant fraction dicriminator, Σ – impedance matched passive summing circuit, SA – spectroscopy amplifier.

Digital CDB spectrometer. Measurements reported in this work were performed using a digital CDB spectrometer described in Ref. [12]. A simplified scheme of the digital CDB spectrometer is shown in Figure 1. The spectrometer is equipped with two HPGe detectors Canberra GC3519 and GC3018 with relative efficiencies of 35 and 30%. The detectors were always positioned face-to-face, see Fig. 1. The source-sample sandwich is located symmetrically between two HPGe detectors in the distance *r* from both detectors and the distance *d* from the common horizontal axis of detectors. Two geometries were used in the measurements described in this work:

(i) *central geometry* with the source-target assembly situated on the common axis of detectors (i.e. $d = 0$) and
(ii) *non-central geometry* when the source-target sandwich is placed at the distance $d = 40$ mm from the common axis of detectors.

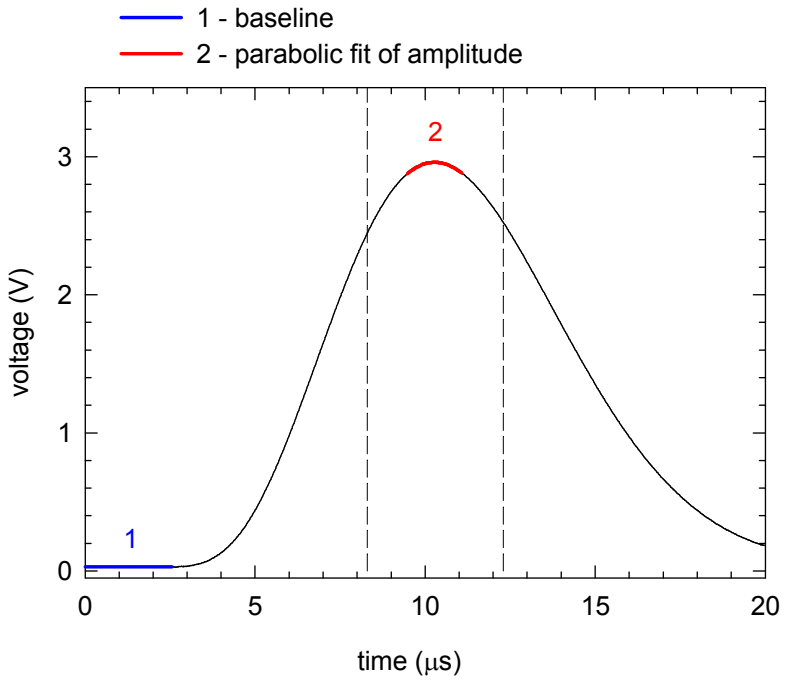

Figure 2 An example of a sampled waveform from the Canberra GC3519 detector. The regions used for determination of the baseline level (1) and for the parabolic fitting of pulse maximum (2) are shown in the figure. Vertical dashes lines show the time window required for positioning the pulse maximum.

Pulses from HPGe detectors are firstly amplified and sharpened using a semi-Gaussian filter (time constant 4 μs) in Canberra 2020 spectroscopy amplifiers (SAs) in order to improve the signal-to-noise ratio. The shaped pulses are sampled in real time by an Acqiris DC 440 two-channel 12-bit digitizer (Aglient Technologies). The digitizer is externally triggered by a timing circuit consisting of Ortec 460 delay line amplifiers (DLAs) which shape detector signals into the form suitable for Ortec 473A constant fraction discriminators (CFDs). Positive logic NIM time signals from CFDs are summed by an impedance-matched passive circuit (Σ) and used as an external trigger signal for the digitizer. As shown schematically in Fig.1, one can select two modes of measurement by setting the trigger level of digitizer:

(i) *single mode*, trigger level (position 1) - a photon detected in one detector starts sampling and data acquisition independently whether a photon was detected simultaneously in the second detector or not;
(ii) *coincidence mode*, trigger level (position 2) set so that it can be exceeded only by a sum of the CFD signals; hence, only a coincidence event, i.e. two photons detected simultaneously in both detectors, can start sampling and data acquisition.

The trigger level of digitizer can be adjusted by a software command. Hence, one can switch between the single and the coincidence mode even during measurement. The CDB measurement is performed in steps called *sessions*. Measurement in sessions allows for digital stabilization which corrects possible drift of the baseline level or the gain of detector pre-amplifier and/or SA. Each session consists of two parts: a single mode measurement with trigger level set to position 1 (see Fig. 1) followed by measurement in the coincidence mode with trigger level set to position 2. The single mode measurement enables to measure not only annihilation gamma rays, but also peak from the secondary photons with intensity sufficient for a precise energy calibration, which is then used in the subsequent measurement in the coincidence mode.

An example of sampled waveform is shown in Fig. 2. Each waveform consists of 1000 points taken with the sampling period of 20 ns. Analysis of sampled waveforms is performed off-line by software using the algorithm depicted schematically in Fig. 3 and described in details in Ref. [12]. The analysis is performed in two steps called runs #1 and #2:

In run #1 the baseline level and the pulse amplitude are determined for each waveform. The baseline level is determined as an average of the background prior to the pulse, while the pulse amplitude is obtained by parabolic fitting of the region containing 40 points around the channel with the maximum number of counts (see Fig. 2). Subsequently, the waveforms are examined by so called *fixed filters*. The purpose of the fixed filters is a raw selection of waveforms and rejection of seriously distorted pulses. Fixed filters are watchdogs which reject waveforms having some of the following deficiencies: (a) the amplitude of the pulse falls outside the vertical range of digitizer, (b) the baseline prior to the pulse exhibits too high rms, (c) parabolic fitting of the pulse amplitude gave too high χ^2 value, i.e. refinement of the pulse maximum failed. Waveforms which do not pass testing by the fixed filters are rejected from further analysis. For waveforms accepted by the shape filters the height of each pulse - calculated as a difference between the baseline and the pulse amplitude - is added to histogram of pulse heights. Subsequently, each waveform is normalized to the same amplitude and shifted in the time scale to set the position of its maximum to a common reference time corresponding to the channel where most waveforms reached their maximum. Note that due to external triggering by a uniform logic signal produced in the timing circuit the maximum is reached at very similar position for most waveforms. A waveform is accepted only if its maximum occurs in the time window ± 2000 ns around the reference point, i.e. any horizontal shift of the waveform, if required, is not higher than 100 points. This time window is indicated in Fig. 2 by vertical dashed lines. An ideal pulse shape is constructed from the normalized waveforms using the most frequent values for each time point. As an example, the ideal waveform shape for the detector Canberra GC3519 is shown in Fig. 4.

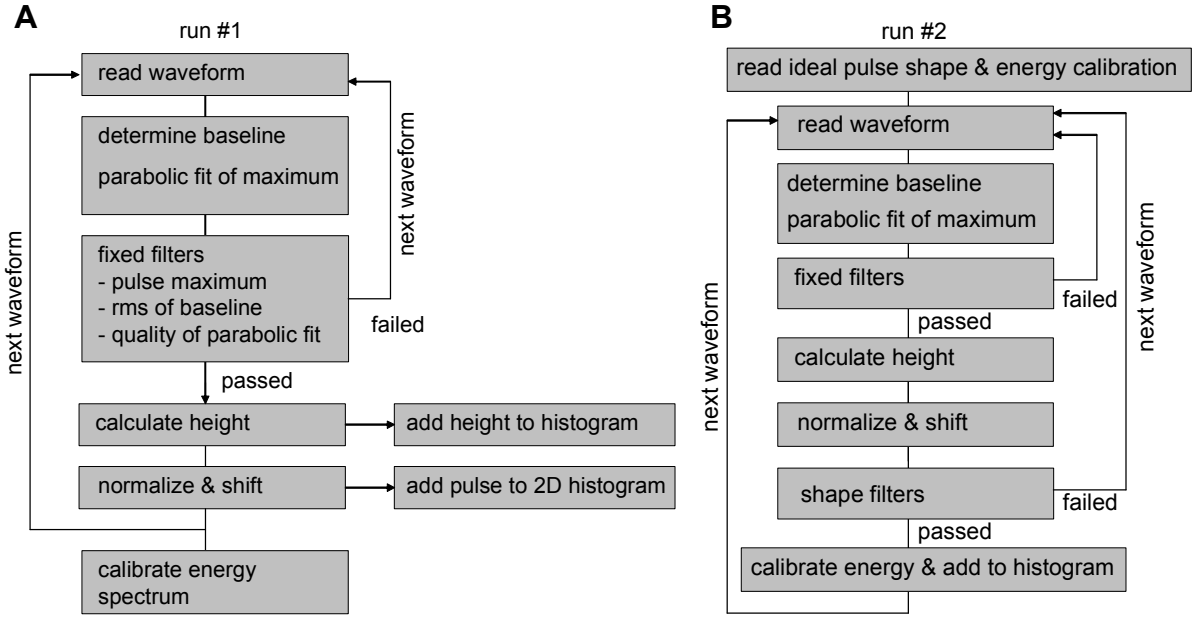

Figure 3 Schematic diagram of the operations performed in the analysis of sampled waveforms in the run #1 (A) and run #2 (B).

Run #1 creates a histogram of pulse heights, which is subsequently calibrated using known energies of the annihilation peak (511keV) and the secondary photon (1274 keV for ^{22}Na) and (1078 keV for ^{68}Ge/^{68}Ga). The energy calibration is performed independently for each session in order to compensate for any possible drift of the baseline level or the gain of detector pre-amplifier and/or SA.

The energy calibration and the ideal pulse shape created in run #1 are used subsequently in run #2. As indicated in Fig. 3B the analysis in the run #2 is performed in the same way as in the run #1, but in addition *shape filters* are applied for fine selection of pulses. The shape of each normalized waveform is compared with the ideal shape determined in run #1. A waveform is accepted only if it everywhere falls within a certain band around the ideal shape. The lower and upper limits of this band are set independently for each channel at positions where the distribution created from normalized waveforms in this channel falls to 1/10 of its maximum.

For clarity in the following text a spectrum constructed in run #1 from all waveforms which passed raw selection by fixed filters will be called a *raw spectrum* to distinguish it from a *filtered spectrum* constructed in run #2 only from waveforms accepted by shape filters.

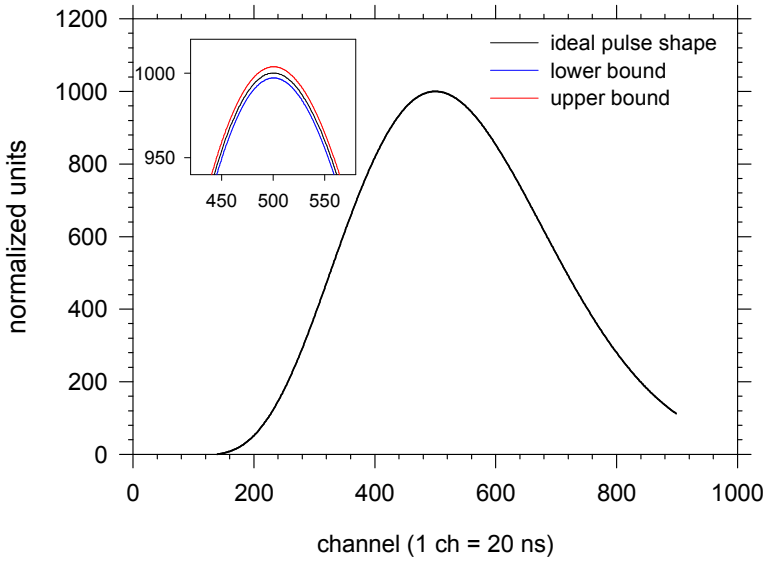

Figure 4 The ideal shape of waveform for HPGe detector Canberra GC3519. The inset shows a zoomed detail around maximum with lower and upper bounds. Note that first 100 and last 100 channels are not used because these channels may not be available due to the horizontal shift of the waveform to a common reference position.

Results and Discussion

^{22}Na positron source. In this sub-section we report results obtained using positrons emitted by ^{22}Na positron source. Fig. 5 shows energy spectra measured by the Canberra GC3519detector. A raw spectrum obtained in the single mode is plotted by a black line, while a raw spectrum measured in the coincidence mode is plotted by a blue line. The spectra in Fig. 5 were normalized to the same total area. The peak located at 511 keV comes from annihilation of thermalized positrons which represents a dominant contribution in the spectrum. The annihilation peak at 511 keV is broadened due to Doppler shift caused by non-zero momentum of electrons which annihilated positrons. Note that momentum of thermalized positron is negligible compared to momentum of electrons. In conventional Doppler broadening spectroscopy shape of the annihilation peak is measured to obtain information about momentum distribution of electrons in the studied sample. However, in case of the annihilation-in-flight events the situation is reversed and positron momentum substantially exceeds the momentum of electrons. The second peak in Fig. 5 located at energy of 1274 keV comes from the secondary gamma rays emitted by the daughter ^{22}Ne nucleus almost simultaneously with the positron. The additional peak located at energy of 1460 keV, which can be seen only in the spectrum measured in the single mode, is a contribution of gamma rays emitted by the ^{40}K radioisotope (half life 1.3 billion years) which is always present in the natural background.

Comparing the spectrum measured in the single and in the coincidence mode on can see that in the coincidence mode the annihilation peak remains unaltered while the peak from the secondary gamma rays (1274 keV) is suppressed and the ^{40}K peak is completely removed. Moreover, the background above the annihilation peak, which comes mainly from the Compton scattering of the

secondary gamma rays, is suppressed in the coincidence mode. If measurement is performed in the coincidence mode, the peak at 1274 keV represents predominantly a contribution of such causal events when the secondary gamma ray is detected in one detector and the corresponding annihilation photon is registered in the second detector while the second annihilation gamma ray escapes undetected. The ^{40}K radioisotope may contribute to the spectrum only in case of a random coincidence with some photon in the second detector. Since probability of such event is extremely low the ^{40}K peak is not visible in the spectrum measured in the coincidence mode.

In addition to photopeaks two summation peaks - denoted 1 and 2 - can be seen in Fig. 5. Peak 1 is located at the energy 2 × 511 keV, corresponding to events when two annihilations occur at very similar time, i.e. so close to each other that they are considered as a single event. The summation peak 2 (511 + 1274 = 1785 keV) comes from events when the annihilation and the secondary gamma ray were detected simultaneously in one detector. The summation peaks 1 and 2 are much more pronounced in the spectrum measured in coincidence mode because both these peaks are produced by coincidence events.

Fig. 5 shows also the effect of the shape filters comparing the raw coincidence spectrum, i.e. the spectrum constructed from all waveforms which passed raw selection by fixed filters (blue line), and the filtered spectrum constructed only from waveforms accepted by the shape filters (red line). It is clear that application of shape filters leads to a further reduction of background which comes mainly from random pile-up of the signal from the annihilation gamma ray with the signal from Compton scattering of some other gamma ray appeared in the detector at similar time.

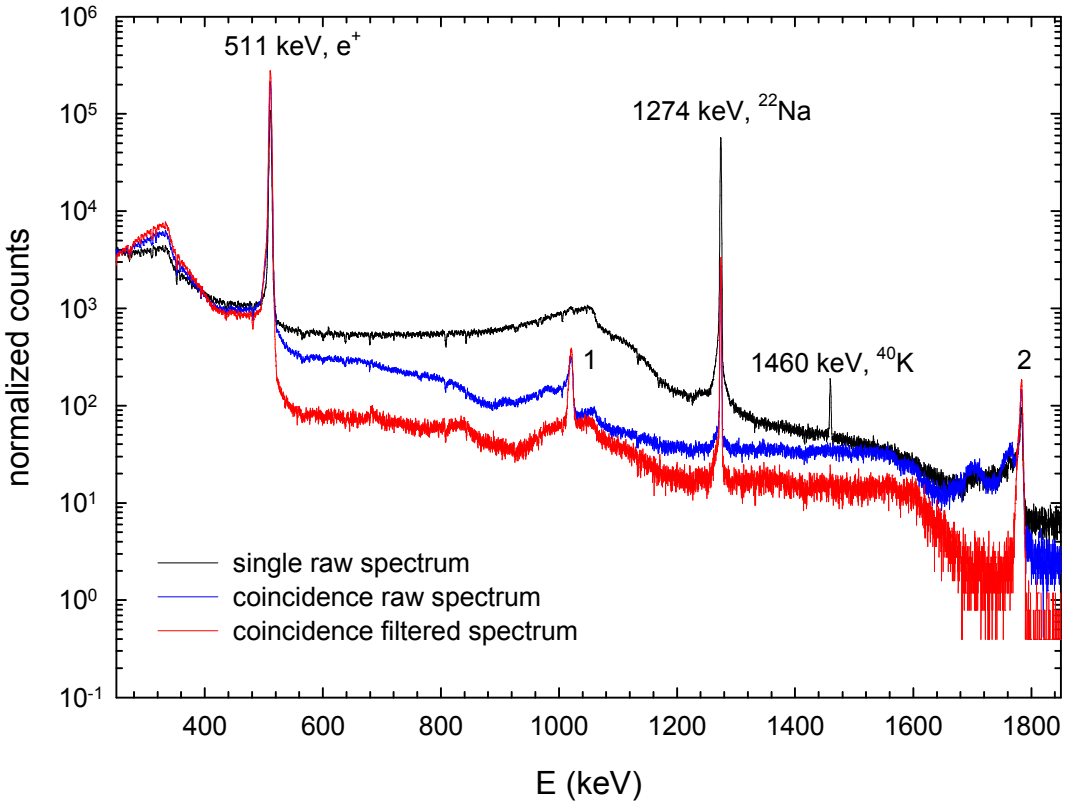

Figure 5 The energy spectrum measured by HPGe detector Canberra GC3519 for positrons emitted by ^{22}Na positron source into Cu target. Three spectra are compared in the figure: raw spectrum measured in the single mode (black line), raw spectrum measured in the coincidence mode (blue line) and filtered spectrum measured in the coincidence mode (red line). All spectra in the figure were measured in the central geometry and were normalized to the same total area. Two summation peaks are denoted in the figure: 1 - two annihilation gamma rays with energy of 511 keV detected simultaneously in one detector, 2 – the annihilation gamma ray (511 keV) and the secondary gamma ray (1274 keV) detected simultaneously in one detector.

The effect of shape filters is clearly visible in Fig. 6, which shows the relative fraction of counts rejected by the shape filters

$$f_{rejected}(E) = \frac{n_{raw}(E) - n_{filtered}(E)}{n_{raw}(E)}, \quad (1)$$

where n_{raw} and $n_{filtered}$ denote the number of counts in the raw and filtered spectrum, respectively, for the energy E. From inspection of Fig. 6 it becomes clear that application of shape filters leads to a strong reduction of background above the annihilation peak. This background suppressed by shape filters is caused by pile-up effects, i.e. random summation of signals which appeared at similar time. Since pile-up pulses are randomly shifted in time with respect to each other the shape of the summed signal is distorted and differs from the ideal pulse shape. On the other hand, in the regions of peaks the relative fraction of rejected pulses is relatively low because peaks are caused by *causal* events which produce signals with the proper shape.

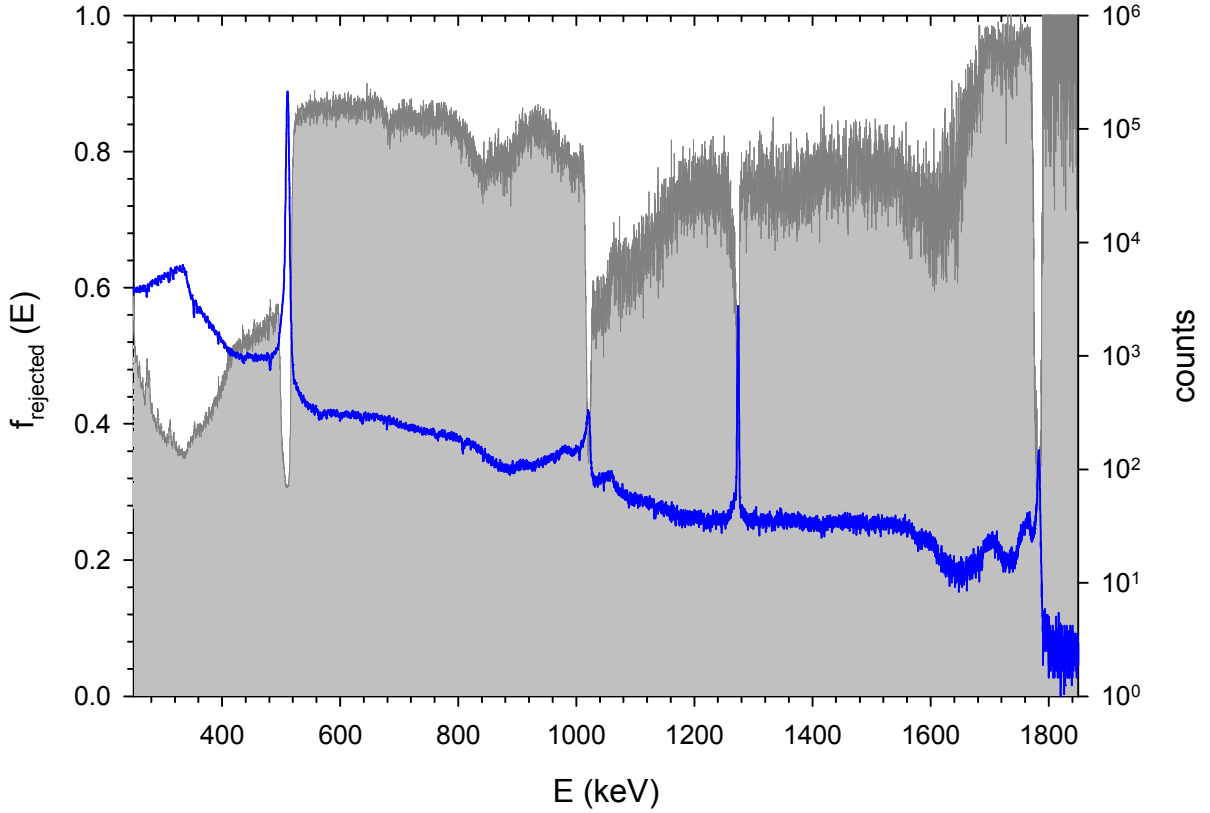

Figure 6 Shadowed area shows the relative fraction $f_{rejected}$ of counts rejected by the shape filters at various energies. The blue line shows filtered energy spectrum for positrons emitted by ^{22}Na source into Cu target measured in the central geometry in the coincidence mode.

Fig. 7 shows color coded two-dimensional CDB spectra, i.e. the sum of gamma ray energies $E_1 + E_2$ determined in both detectors plotted versus the difference of these energies $E_1 - E_2$, measured in the central geometry. The raw and the filtered two-dimensional CDB spectrum are plotted in Figs. 7A and 7B, respectively. Several features can be clearly seen in the CDB spectra:

(i) *a dominant annihilation peak* centered at $E_1 + E_2 = 2 \times 511$ keV and $E_1 + E_2 = 0$ which comes from annihilation of thermalized positrons;

(ii) *diagonal ridges* crossing each other at the annihilation peak.

The diagonal ridges *below* the annihilation peak come from events when annihilation gamma ray was detected in one detector, while in the second detector the annihilation photon deposited only part of its energy due to Compton scattering.

The diagonal ridges *above* the annihilation peak are caused by events when the annihilation gamma ray was registered in one detector while in the second detector the annihilation gamma ray was summed with Compton scattered secondary photon.

(iii) *peaks located on the vertical line* $E_1 + E_2 = 0$ above the annihilation peak come from random coincidences, i.e. events when gamma rays from two independent events occurring in similar time are registered as a single event. The peaks correspond to cases when gamma rays deposited full energy in both detectors, while the ridges crossing each other at the peak position are caused by events when one photon undergone Compton scattering and deposited only part of its energy in detector.

(iv) *horizontal lines or streaks* are caused by Compton scattering of a single gamma ray between the detectors, i.e. gamma ray backscattered in one detector is registered in the second detector. Streaks from scattering of 511 keV and 1274 keV gamma ray between detectors can bee seen in Fig. 7.

(v) *hyperbolic contribution* around the annihilation peak which represents a contribution of positrons annihilated in-flight.

From inspection of Fig. 7 it is clear that application of shape filters suppresses the background caused by random pile-up effects, while features caused by causal effects remain unchanged in the filtered spectrum.

The vertical cut at $E_1 - E_2 = 0$ and the horizontal cut at $E_1 + E_2 = 2 \times 511$ keV from the two-dimensional CDB spectra are plotted in Figure 8A and 8B, respectively. The main contribution to CDB spectra comes from annihilation of thermalized positrons (peak 1). The additional peak (2) which is located at $E_1 + E_2 = 4 \times 511$ keV represents a contribution of 'four photon' events where two independent annihilations of thermalized positron occurred in so short time interval that they are considered as a single event. Since two annihilation photons were detected in each detector the sum of energy deposited in detectors equals four times the rest electron mass. The maximum of a waveform formed by a superposition of pulses from two independent annihilations corresponds to energy of 4×511 keV only when both events occur almost simultaneously, i.e. within very short time interval compared to the pulse duration. Waveforms formed by random summation of annihilation events which appeared within longer time interval exhibit maximum which is lower since pulses from these two annihilation events are shifted in time with respect to each other. As a consequence the peak at $E_1 + E_2 = 4 \times 511$ keV is preceded by a slowly decaying tail, see Fig. 8A. Since this contribution is caused by annihilation of thermalized positrons the difference of gamma ray energies is very small and the contribution appears in two-dimensional CDB spectra in Fig. 7A as a vertical line. An abrupt drop of this tail which can be observed at $E_1 + E_2 \approx 1850$ KeV occurs when the time distance between two annihilation events becomes so large that horizontal shift of the maximum of superimposed waveform exceeds 100 channels (2000 ns) and such events are rejected by fixed filters already in run #1. Peak (3) located at energy $E_1 + E_2 = 2 \times 1274$ keV is caused by random coincidences of two secondary photons while the last peak (4) at energy $E_1 + E_2 = 4 \times 511 + 2 \times 1274$ keV is a 'full absorption peak' caused by random coincidences of two annihilation events when all four annihilation gamma rays and both secondary photons are detected.

The central peak (1) in Fig. 8B represents a contribution of annihilations of thermalized positrons. The side peaks (5) in Fig. 8B are due to Compton scattering when one annihilation gamma ray is backscattered from one detector into the second detector. Since the backscattered annihilation gamma ray (scattering angle 180^o) deposits 340.7 keV in one detector (Compton edge) and carries out 170.3 keV which is then deposited in the second detector, the energy difference between the two detectors is $2 \times 170.3 = 340.6$ keV which corresponds to the maxima of the side peaks in Fig. 8B. One can see in Fig. 8B that application of shape filters leads to a significant reduction of background around the central annihilation peak. However, side peaks caused by backscattered gamma rays remain unaltered since this is a causal effect which produces pulses of proper shape.

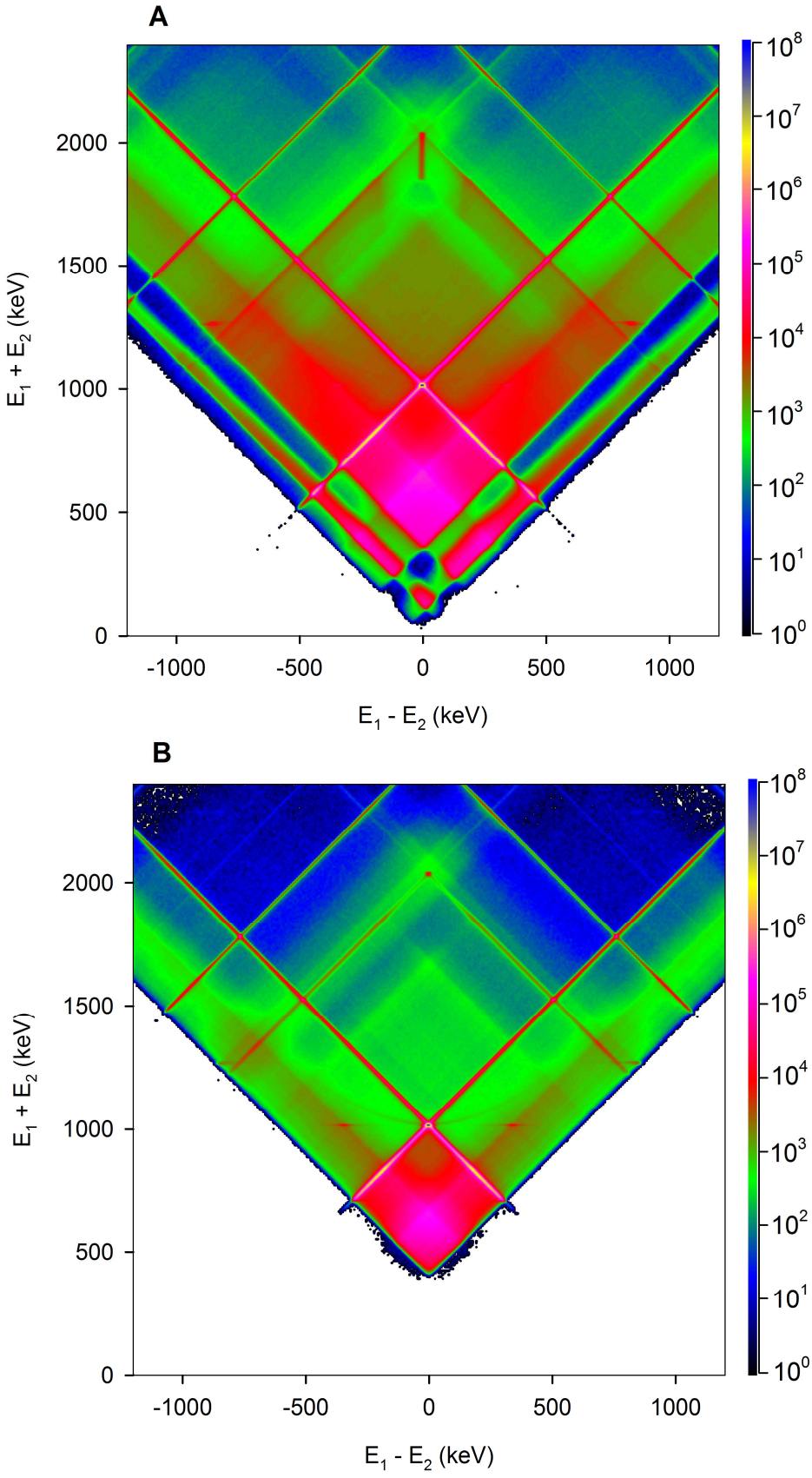

Figure 7 Color coded two dimensional CDB spectra measured in the central geometry for positrons emitted by ^{22}Na source into Cu target: (A) raw spectrum, (B) filtered spectrum.

The TQAF contribution with hyperbolic shape is clearly visible in Fig. 9A which shows a detail of the region around the annihilation peak in the filtered CDB spectrum from Fig. 7B. Let us

consider a TQAF process where a positron with total energy E_+ and momentum $\boldsymbol{p}_+$ is annihilated by electron at rest with emission of two gamma quanta with energies E_1 and E_2. From the energy conservation law it follows

$$E_+ + m_0c^2 = E_1 + E_2 + E_B, \tag{2}$$

where m_0 is the electron rest mass, c is the velocity of light and E_B is the electron binding energy in the matter. Since E_B is very small compared to the energy of non-thermalized positron in was neglected in further calculations. The conservation of momentum can be expressed as

$$p_+^2c^2 = E_1^2 + E_2^2 + 2E_1E_2\cos\theta\,, \tag{3}$$

where θ is the angle between the emitted gamma rays, see Fig. 1. Combining Eqs. (2), (3) and using the well known relativistic equation $E_+^2 = m_0^2c^4 + p^2c^2$ one obtains a relation which relates the energies E_1, E_2 of annihilation gamma rays with the angle θ between them:

$$\frac{1}{E_1} + \frac{1}{E_2} = \frac{1-\cos\theta}{m_0c^2}. \tag{4}$$

For comparison with an experimental CDB spectrum (i.e. $E_1 + E_2$ plotted versus $E_1 - E_2$) it is more convenient to rewrite Eq. (4) in the form

$$E_1 + E_2 = \sqrt{(E_1 - E_2)^2 + \left(\frac{2m_0c^2}{1-\cos\theta}\right)^2} + \frac{2m_0c^2}{1-\cos\theta}, \tag{5}$$

which relates the sum $E_1 + E_2$ with the difference $E_1 - E_2$. For a fixed angle θ the curve described by Eq. (5) has a hyperbolic shape with minimum occurring at $E_1 - E_2 = 0$. The vertical position of the minimum is located at

$$(E_1 + E_2)_{\min} = \frac{4m_0c^2}{1-\cos\theta}. \tag{6}$$

Hence, for $\theta = 180^o$ Eq. (5) gives $(E_1 + E_2)_{\min} = 2m_0c^2$ and the minimum is located at the annihilation peak. With decreasing angle θ the TQAF hyperbola is gradually shifted up, i.e. to higher energies. The minimum angle θ_{min} between annihilation gamma rays is determined by the end-point-energy of emitted positrons $T_{+,f}$. Obviously, $E_1 + E_2$ cannot be higher than $T_{+,f} + 2m_0c^2$ which implies that the minimum angle between the annihilation gamma rays is given by the relation

$$(\cos\theta)_{\min} = \frac{T_{+,f} - 2m_0c^2}{T_{+,f} + 2m_0c^2}. \tag{7}$$

In the case of a ^{22}Na radioisotope emitting positrons with the end-point energy $T_{+,f} = 545$ keV the angle between the annihilation gamma rays cannot be smaller than $\theta_{min} = 107.7^o$, while for ^{68}Ge/^{68}Ga which produces positrons with $T_{+,f} = 1897$ keV the minimum angle between the annihilation gamma rays is $\theta_{min} = 72.5^o$. Hence, the annihilation gamma rays may be always collinear, but the deviation from collinearity cannot exceed $180^o - \theta_{min}$.

In the CDB spectrometer the HPGe detectors are oriented face-to-face, see Fig. 1. This configuration limits the TQAF contribution to the CDB spectrum only to events with a constant angle θ determined by the distance d of positron source from the common axis of detectors. In the central geometry ($d = 0$) only anti-collinear TQAF photons ($\theta = 180^o - \Delta\theta$) are registered. Here, $\Delta\theta = 2\arctan(\phi/2r)$ is the deviation from the 180^o angle for which the TQAF photons can be still registered because of the finite size of HPGe detectors having diameter ϕ. In our case $\Delta\theta \approx 10^o$, i.e. gamma rays emitted with angles θ in the range from 180^o to 170^o can be detected. This corresponds to the width of TQAF hyperbola of ≈ 8 keV. Fig. 9B shows a comparison of the filtered experimental CDB spectrum with the theoretical curves calculated by Eq. (5) for positrons emitted by ^{22}Na radioisotope and angles between the annihilation gamma rays $\theta = 180^o$ and 170^o. Obviously the band defined by the theoretical curves in Fig. 9B agrees very well with shape of the TQAF contribution determined experimentally.

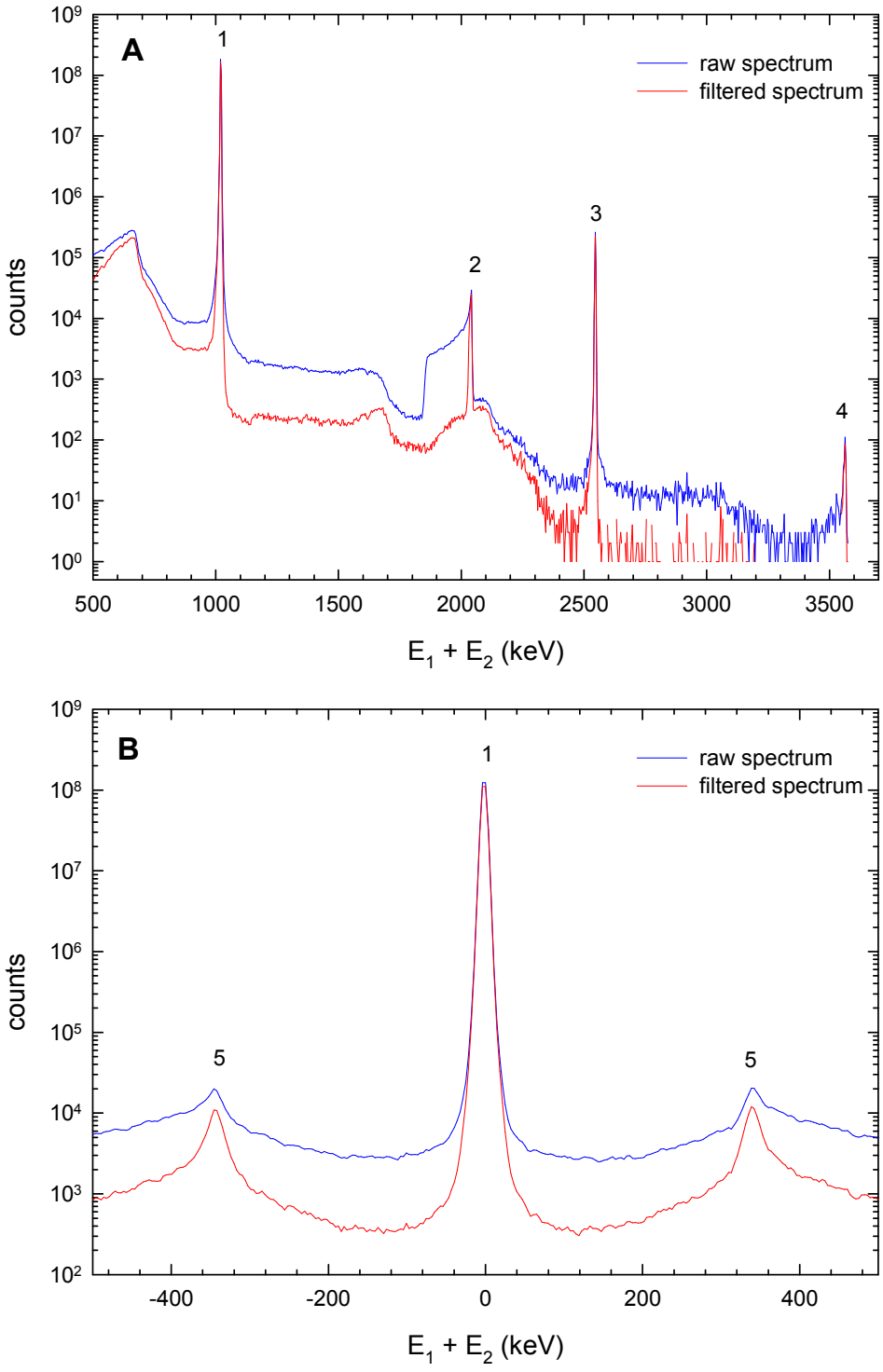

Figure 8 Vertical cut at $E_1 - E_2 = 0$ (A) and horizontal cut at $E_1 + E_2 = 2 \times 511$ keV (B) from two dimensional spectra in Fig. 7. Cuts from the raw spectrum are plotted by the blue line, while cuts from the filtered spectra are plotted by the red line. Several peaks can be recognized in the vertical cut in Fig. 8A: 1 – annihilation peak (2 × 511 keV) , 2 – 'four photon' peak (4 × 511 keV), representing a random coincidence of two annihilation photons registered in both detectors, 3 – random coincidence of two secondary photons (2 × 1274 keV), 4 – 'full absorption peak' (4 × 511 + 2 × 1274 keV) representing a random coincidence of two annihilation events when both annihilation gamma rays and both secondary photons were detected. The horizontal cut in Fig. 8B exhibits the annihilation peak (1) and two backscattering peaks (5).

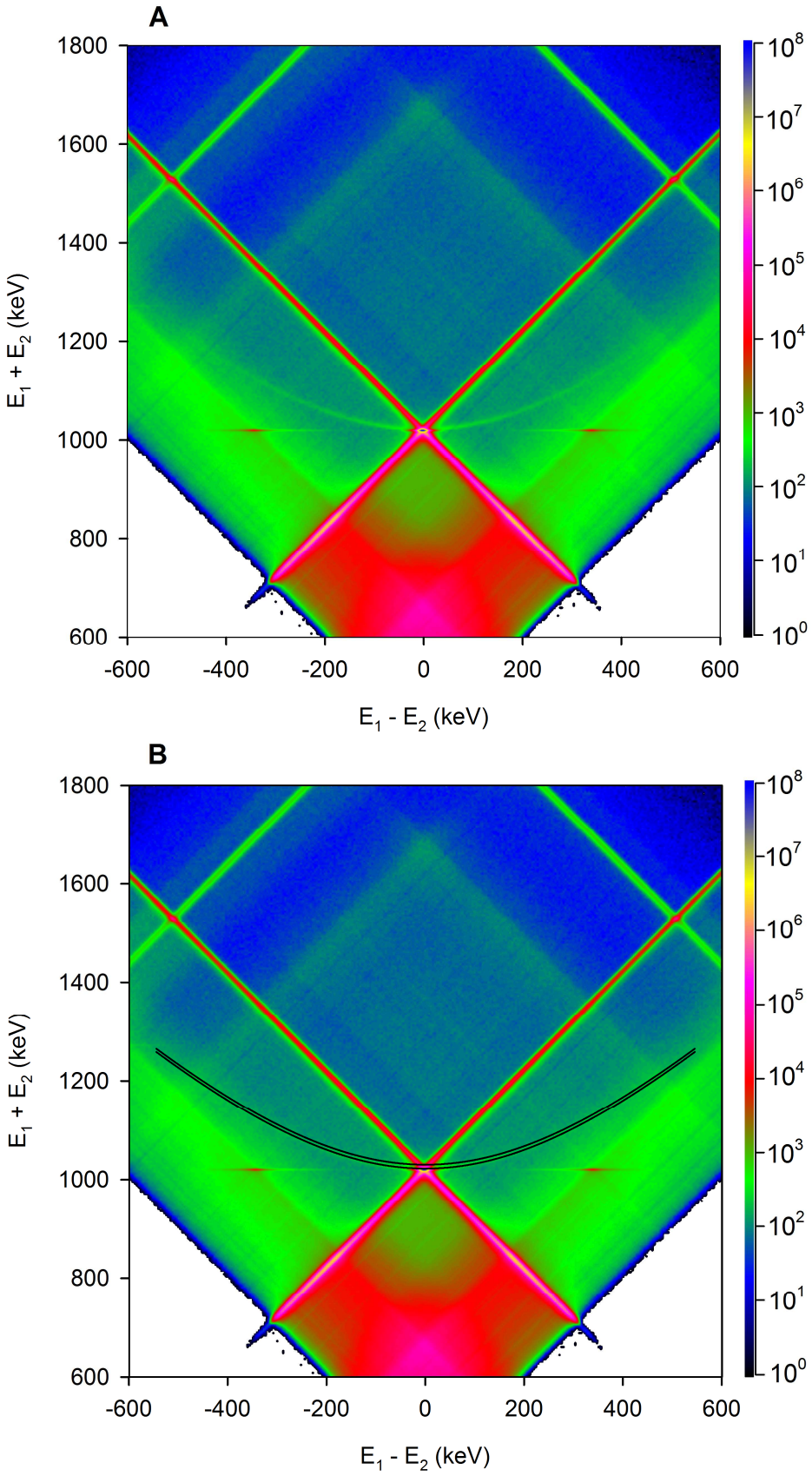

Figure 9 Filtered two dimensional CDB spectrum measured in the central geometry for positrons emitted by ^{22}Na source into Cu target: a detail of the region around the annihilation peak. (A) experimental spectrum, (B) experimental spectrum compared with the theoretical curves calculated by Eq. (5) for angles between the annihilation gamma rays $\theta = 180^{o}$ and 170^{o}.

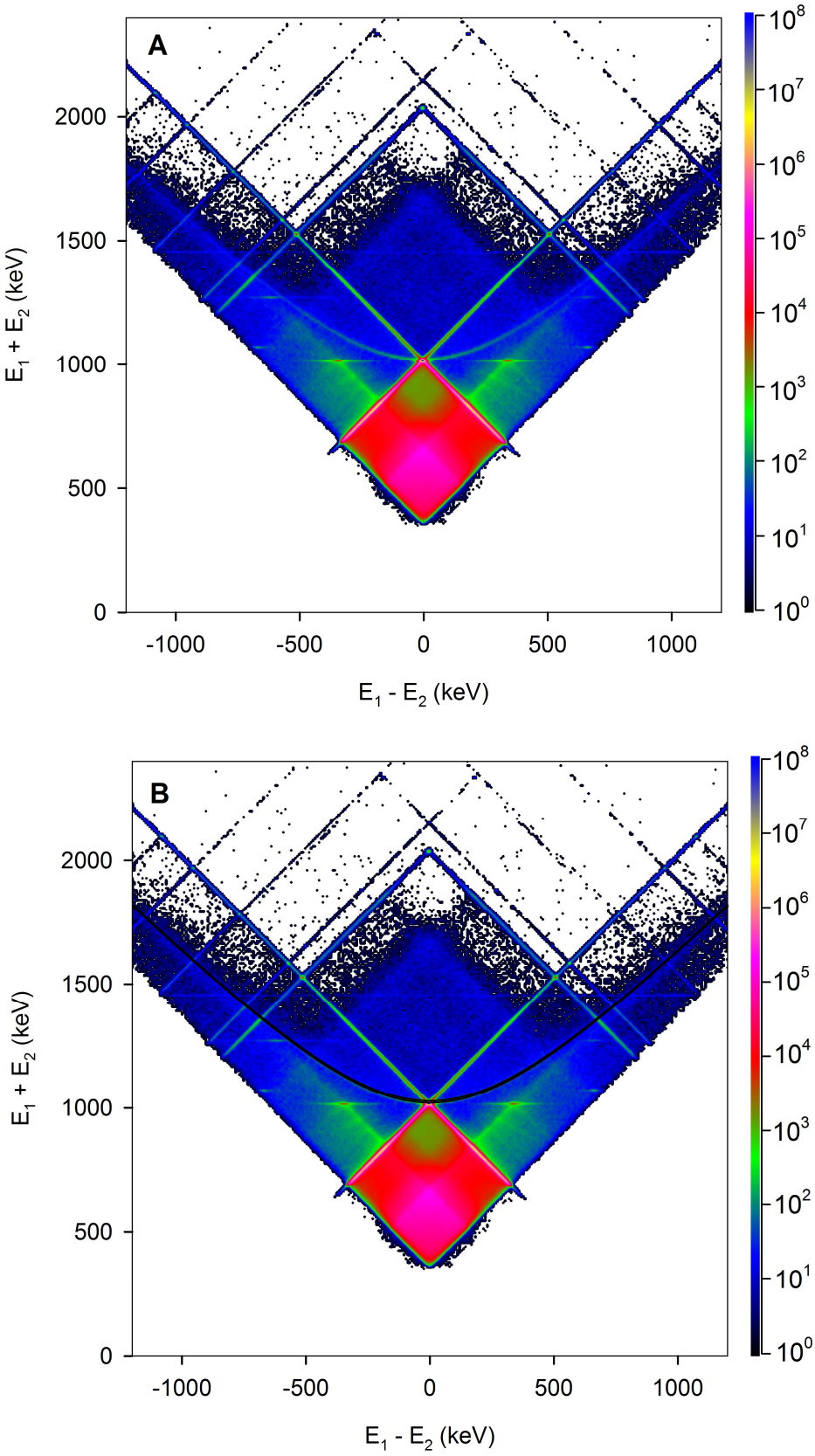

Figure 10 Filtered two dimensional CDB spectrum measured in the central geometry for positrons emitted by ^{68}Ge/^{68}Ga source into Mg target (A) experimental spectrum, (B) experimental spectrum compared by theoretical curve calculated by Eq. (5) for angles between the annihilation gamma rays $\theta = 180^{o}$ and 170^{o}.

^{68}Ge/^{68}Ga positron source. Results for positrons emitted by a ^{68}Ge/^{68}Ga source are presented in this sub-section. Fig. 10 shows the filtered two dimensional CDB spectrum for positrons emitted by ^{68}Ge/^{68}Ga source into Mg target. The measurement was performed in the same central geometry as the measurement with ^{22}Na source described in the previous sub-section. One can see in Fig. 10 that compared to the previous measurement with ^{22}Na source the CDB spectrum obtained with ^{68}Ge/^{68}Ga positron generator exhibits a lower background due to low probability of secondary photon emission by ^{68}Ga radioisotope. Moreover, because of higher end-point-energy of positrons emitted by ^{68}Ga the TQAF the hyperbolic contribution extends to significantly higher energies than in the case of the ^{22}Na source. In Fig. 10B the experimental CDB spectrum is compared with the theoretical TQAF curves calculated by Eq. (5) for the angle between the annihilation gamma rays θ = 180^o and 170^o. From inspection of Fig. 10B it is clear that the theoretical curves agree well with TQAF contribution measured in experiment.

Because of low background it is possible to see in Fig. 10A a horizontal line at the energy E_1 + E_2 =1461 keV which is caused by scattering of gamma ray with energy of 1461 keV between the detectors. The gamma rays with energy of 1461 keV are emitted by ^{40}K radioisotope with half life of 1.3 billion years which is always present in natural background. Since ^{40}K is present in the floor, ceiling and walls surrounding the spectrometer the gamma rays with energies of 1461 keV strike detectors at various incident angles. The scattering angle for which the ^{40}K photon Compton scattered in one detector photon falls into the second detector and also the energy deposited in the first and the second detector vary for various incident angles. Since all incident angles are possible a continuous horizontal line caused by Compton scattering of ^{40}K gamma under various scattering angles cab be seen in the CDB spectrum in Fig. 10A. On the other hand, in the central geometry ($r >> \phi$) the annihilation gamma ray hits the detector in the direction which is parallel to the horizontal detector axis or has only a little deviation from it. Hence, an annihilation gamma ray Compton scattered in one detector can be registered in the second detector only if the scattering angle was close to 180^o (backscattering). As a consequence scattering of annihilation gamma rays between detectors appears in Fig. 10A as horizontal streaks at energy $E_1 + E_2 = 2 \times 511$ keV. These streaks are caused by annihilations of thermalized positrons when one annihilation gamma ray deposited full energy in the first detector, while the second annihilation photon was backscattered in the second detector and hit the first detector.

Vertical (at $E_1 - E_2 = 0$) and horizontal ($E_1 + E_2 = 2 \times 511$ keV) cuts from the two-dimensional CDB spectrum in Fig. 10 are plotted in Fig. 11A and 11B, respectively. The main peak (1) in Fig. 10A located at $E_1 + E_2 = 2 \times 511$ keV represents a contribution of annihilation of thermalized positrons. Two additional peaks which can be seen in Fig. 11B come from random summations: peak (2) located at energy $E_1 + E_2 = 4 \times 511$ keV is the 'four annihilation' peak caused by events when two annihilations took place in similar time and are considered as a single event and two annihilation photons are registered in both detectors; peak (3) located at the energy $E_1 + E_2 = 2 \times$ 1078 keV comes from of random coincidences of the secondary photons with energy of 1078 keV emitted by ^{68}Ga. The main peak (1) in Fig. 11B located at $E_1 - E_2 = 0$ is the Doppler broadened annihilation peak representing a contribution of thermalized positrons. In addition there are also side peaks (4) from events when one annihilation gamma ray deposited full energy in one detector while the second annihilation gamma ray was backscattered between detectors.

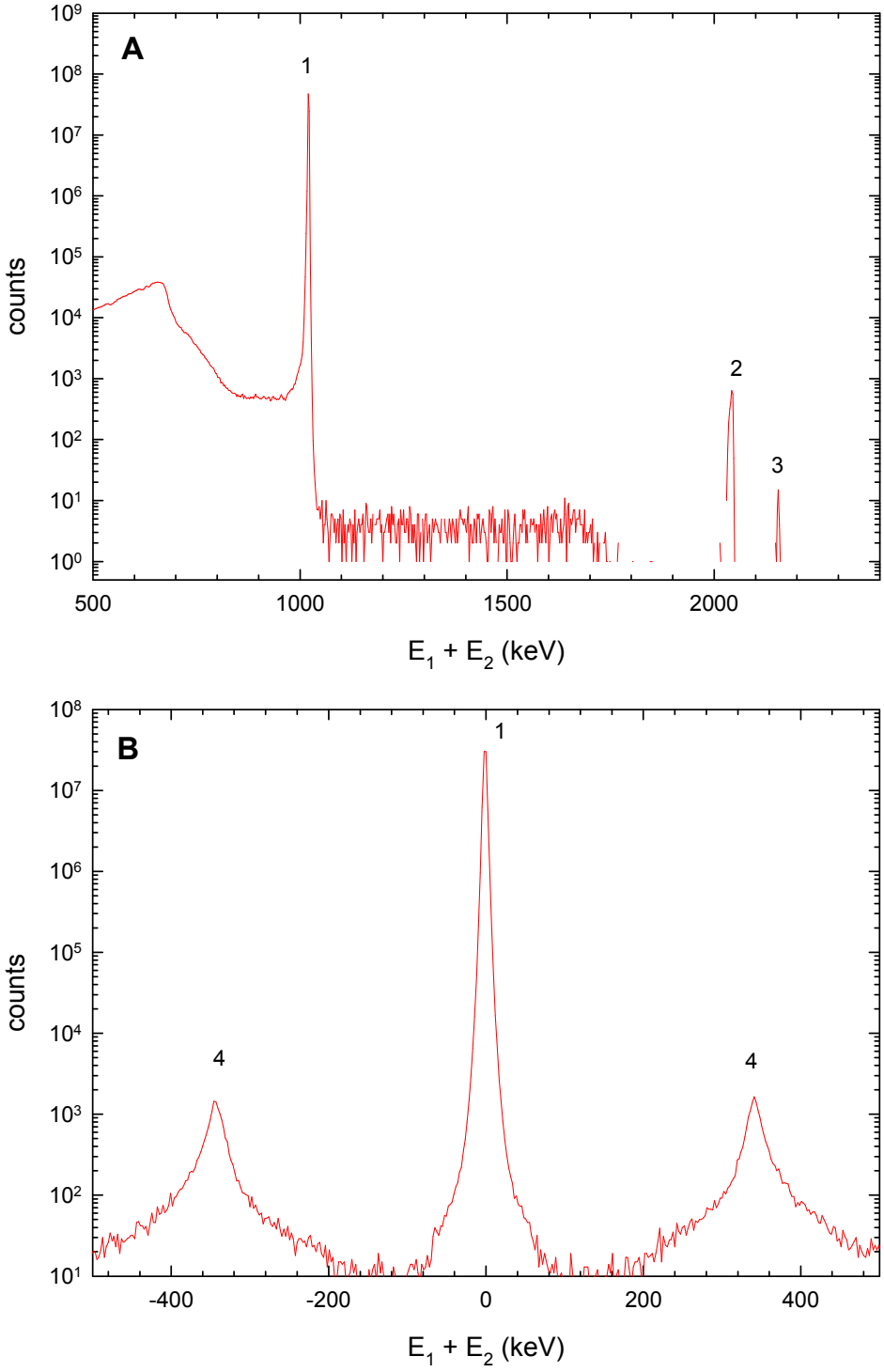

Figure 11 (A) Vertical cut at E_1 - E_2 = 0 and (B) horizontal cut at E_1 + E_2 = 2 × 511 keV from filtered two dimensional spectrum in Fig. 10. The following peaks can be seen in Fig. 11A: 1 – annihilation peak (2 × 511 keV, contribution of thermalized positrons), 2 – 'four photon' peak (4 × 511 keV), representing a random coincidences of two annihilation photons registered in both detectors, 3 – random coincidences of two secondary photons (2 × 1078 keV). The horizontal cut in Fig. 11B contains Doppler broadened main annihilation peak (1) and two backscattering peaks (4).

Measurement in the non-central geometry. This sub-section presents results of additional measurements with positrons emitted by ^{68}Ge/^{68}Ga source into Mg target. The source-target assembly was positioned in the non-central geometry shown in Fig. 12.

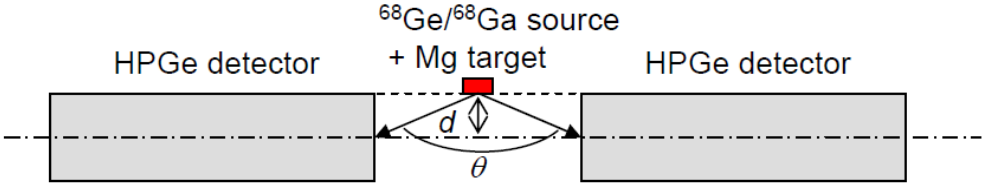

Figure 12 Schematic depiction of the non-central geometry. The distance of the positron source and Mg target from the common axis of detectors was d = 40 mm.

Fig. 13 shows the filtered two dimensional CDB spectrum measured in the non-central geometry. From Eq. (5) it follows that with decreasing angle θ between the annihilation gamma rays the hyperbolic TQAF contribution is shifted up in vertical direction to higher energies. Indeed, one can see in Fig. 13 that the TQAF contribution is positioned above the annihilation peak. From the geometry in Fig. 12 it follows that TQAF gamma rays having angles θ from 160^o to 175^o can be registered in detectors. The theoretical TQAF curves calculated by Eq. (5) for these angles plotted in Fig. 13B are obviously in a good agreement with experiment.

In the non-central geometry shown in Fig. 12 the anti-collinear gamma rays emitted in annihilation of a thermalized positron cannot be detected simultaneously in both detectors. Hence, the annihilation peak in Fig. 13 located at $E_1 - E_2 = 0$ and $E_1 + E_2 = 2 \times 511$ keV is now caused only by gamma rays from two *independent* annihilation events of thermalized positrons occurring so close to each other that they are considered as a single event. Because of this reason the intensity of the annihilation peak in Fig. 13 is significantly lower than in previous measurements performed in the central geometry. Fig. 14A shows a detail of the annihilation peak measured in the central geometry (the whole spectrum is shown in Fig. 10), while Fig. 14B shows detail of the annihilation peak measured in the non-central geometry (the whole spectrum is shown in Fig. 13). The annihilation peak in Fig. 14A measured in the central geometry is broadened due to Doppler shift, which increases energy of one annihilation gamma ray and decreases energy of the second one emitted to the opposite direction. However, no Doppler broadening can be seen in the annihilation peak measured in the non-central geometry because it is caused by random coincidences of gamma rays from independent annihilation events.

Fig. 14 shows a detail of the vertical cut at $E_1 - E_2 = 0$ from the two dimensional CDB spectrum in Fig. 13 for the region around the annihilation peak. The main annihilation peak (1) comes from random coincidences of annihilation gamma rays emitted in two independent annihilations of thermalized positron. Two additional peaks (2) and (3) can be seen above the annihilation peak. The narrow peak (3) is caused by backscattering of the ^{68}Ga secondary photon with energy of 1078 keV between detectors. The broader peak (2) represents a contribution from positron annihilation-in-flight (i.e. the minimum of the TQAF hyperbolic contribution visible in Fig. 13), which is in non-central geometry clearly separated from the main annihilation peak.

Further investigations proposed. Results described in the previous sub-sections clearly demonstrate that the ^{68}Ge/^{68}Ga positron generator is more suitable for investigation of TQAF process than ^{22}Na positron source due to higher end-point-energy of emitted positrons which enables to investigate TQAF contribution in more extended range of energies and also due to the low probability of secondary photon emission, which guarantees almost zero background in the high energy range.

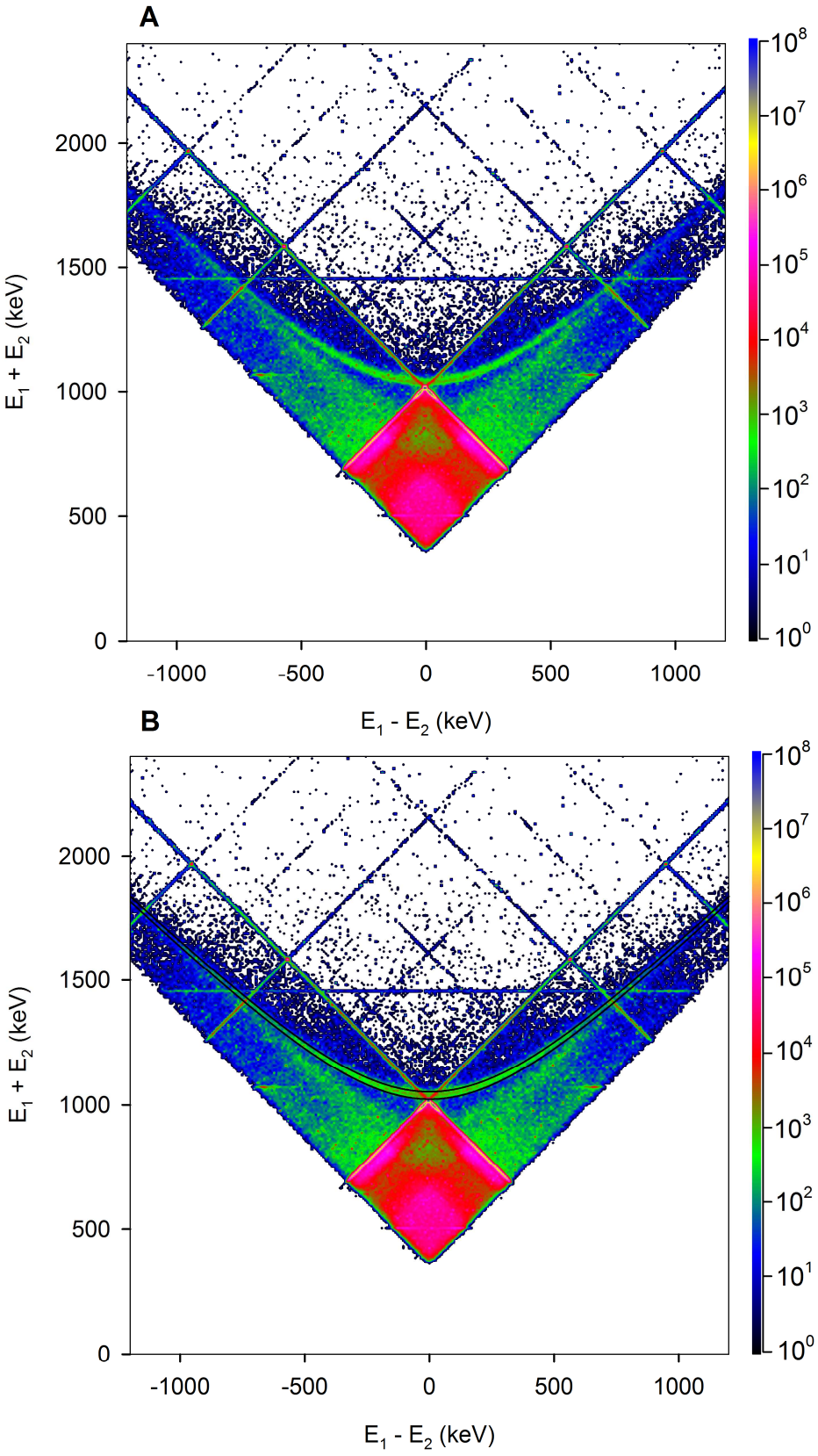

Figure 13 Filtered two dimensional CDB spectrum for positrons emitted by ^{68}Ge/^{68}Ga source into Mg target. The spectrum was measured in the non-central geometry shown schematically in Fig. 12. (A) experimental spectrum, (B) experimental spectrum compared with the theoretical curve calculated by Eq. (5) for the angle between annihilation gamma rays $\theta = 160^o$ and 175^o.

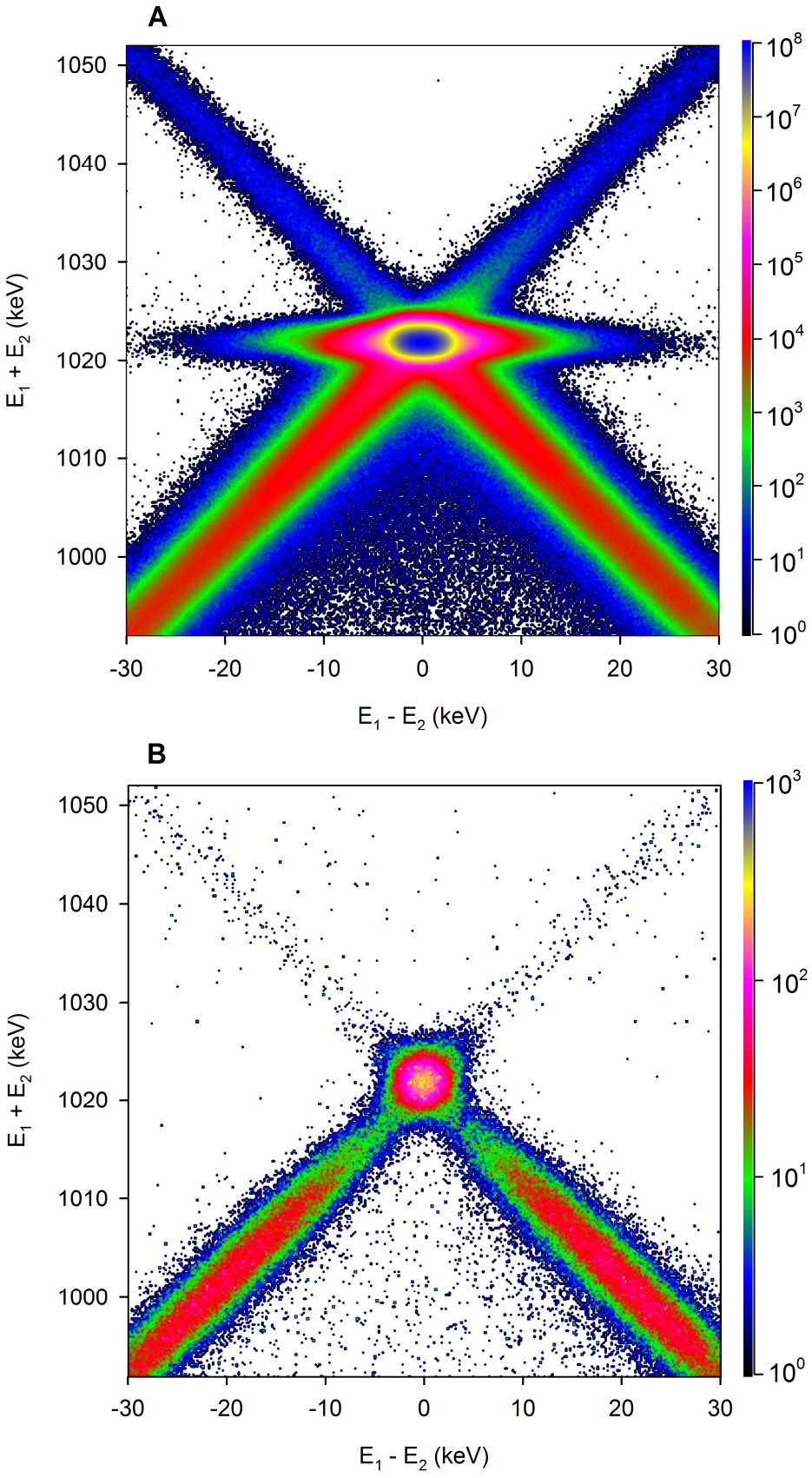

Figure 14 Detail of the annihilation peak in filtered two dimensional CDB spectra for positrons emitted by ^{68}Ge/^{68}Ga source and implanted into Mg target: (A) measurement performed in the central geometry (whole spectrum is plotted in Fig. 10A); (B) measurement performed in the non-central geometry (d = 40 mm, whole spectrum is plotted in Fig. 13A).

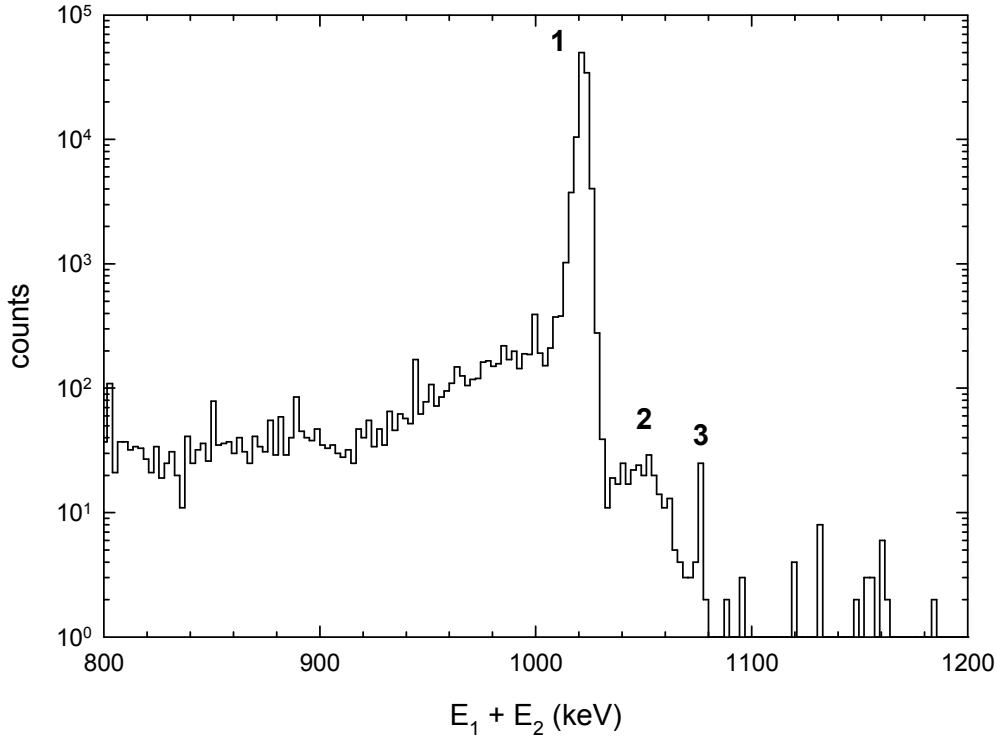

Figure 15 Vertical cut at $E_1 - E_2 = 0$ from the two-dimensional CDB spectrum shown in Fig. 13A: a detail in the energy range around the annihilation peak.

An electron bremsstrahlung gamma-induced positron source (GiPS) has been recently built on the superconducting electron accelerator ELBE at the Helmholtz-Zentrum Dresden-Rossendorf [13,14]. GiPS produces positrons with energy up to 16 MeV. Fig. 16 shows the TQAF contribution calculated by Eq. (5) for positrons produced by ^{22}Na, ^{68}Ge/^{68}Ga and GiPS. The angle between annihilation gamma rays was fixed at $\theta = 180^{o}$ corresponding to the central geometry. One can see in Fig. 16 that GiPS is very suitable tool for study of positron annihilation-in-flight because it enables to investigate the TQAF process in significantly extended energy range compared to the conventional positron sources (8 and 29 times higher than in the case of ^{68}Ge/^{68}Ga and ^{22}Na, respectively). In our recent paper [15] the TQAF cross section for positrons with energies up to 1897 keV was determined from analysis of the profile of the hyperbolic TQAF contribution in two dimensional CDB spectra. It was found that dependence of the TQAF cross-section on the kinetic energy of positron agrees well with the prediction given by QED. Moreover, from comparison of measurements performed on various targets it was concluded that the probability for TQAF is determined predominantly by positron energy and varies only slightly with the target material. Proposed digital CDB measurements with GiPS enable the extension of the energy range in which the TQAF cross section is determined up to 16 MeV.

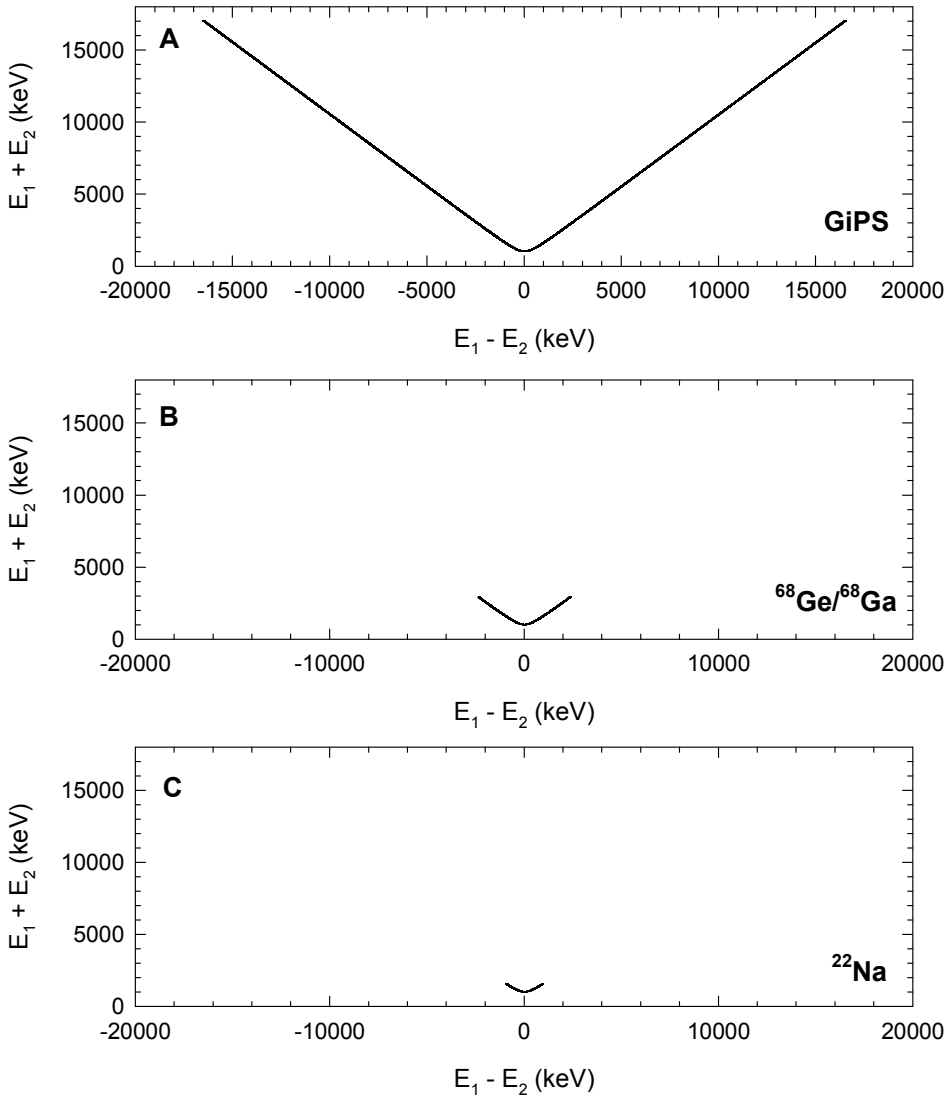

Figure 16 TQAF contributions to two dimensional CDB spectra calculated by Eq. (5) for various positron sources (A) GiPS, (B) ^{68}Ge/^{68}Ga, (C) ^{22}Na. The curves were calculated for the angle between annihilation gamma rays $\theta = 180^{o}$.

Conclusions

The digital CDB spectrometer is an excellent tool for low background measurement of gamma ray coincidences. In this work the spectrometer was employed for investigation of TQAF process for positrons emitted by ^{22}Na and ^{68}Ge/^{68}Ga. The hyperbolic-like shape of TQAF contribution which was clearly resolved in two-dimensional CDB spectra for both radioisotopes agrees well with the theoretical shape given by the special theory of relativity. For investigation of TQAF process the ^{68}Ge/^{68}Ga positron generator is more suitable than ^{22}Na due to the higher end-point-energy of emitted positrons and low probability of secondary photon emission. For further extended investigations of TQAF process an experiment based on digital CDB measurement on the brehmsstrahlung gamma-induced positron source at the superconducting electron accelerator ELBE was proposed. Study of the TQAF process performed in this work is only one example of application of the digital CDB spectrometer. The spectrometer can be further employed for investigation of exotic multi-photon decay modes of various radioisotopes.

Acknowledgement

This work was supported by the Czech Science Foundation (project P108/10/0648) and by the grant SVV-2010-265303.

References

[1] A. Perkins, J. P. Carbotte, Effect of the Positron-Phonon Interaction on Positron Motion, Phys. Rev. B 1 (1970) 101-107.

[2] P. Kubica, A.T. Stewart, Thermalization of Positrons and Positronium, Phys. Rev. Lett. 34 (1975) 852-855.

[3] E. Fernandez et al., Tests of quantum electrodynamics with two-, three-, and four-photon final states from e^+e^- annihilation at $\sqrt{s}$ =29 GeV, Phys. Rev. D 35 (1987) 1-9.

[4] S.H. Connell, R.W. Fearick, R.F.A. Hoernlé , E. Sideras-Haddad, J.P.F. Sellschop, Search for Low-Energy Resonances in the Electron-Positron Annihilation-in-Flight Photon Spectrum, Phys. Rev. Lett. 60 (1988) 2242-2245.

[5] S.A. Colgate, F.C. Gilbert, Electron-Positron Annihilation in Flight, Phys. Rev. 89 (1953) 790-792.

[6] H.W. Kendall, M. Deutsch, Annihilation of Positrons in Flight, Phys. Rev. 101 (1956) 20-26.

[7] B. Adeva et al., Test of QED in e^+e^-, $\gamma\gamma$ at LEP, Phys. Lett. B 250 (1990) 199-204.

[8] M.Z. Akrawy et al., Measurement of the cross sections of the reactions $e^+e^- \rightarrow \gamma\gamma$ and $e^+e^- \rightarrow \gamma\gamma\gamma$ at LEP, Phys. Lett. B 257 (1991) 531-540.

[9] K.G. Lynn, J.R. MacDonald, R.A. Boie, L.C. Feldman, J.D. Gabbe, M.F. Robbins, E. Bonderup, J.A. Golovchenko, Positron-Annihilation Momentum Profiles in Aluminum: Core Contribution and the Independent-Particle Model, Phys. Rev. Lett. 38 (1977) 241-244.

[10] M.H. Weber, A.W. Hunt, J.A. Golovchenko, K.G. Lynn, Energy-Resolved Positron Annihilation in Flight in Solid Targets, Phys. Rev. Lett. 83 (1999) 4658-4661.

[11] A.W. Hunt, D.B. Cassidy, P.A. Sterne, T.E. Cowan, R.H. Howel, K.G. Lynn, J.A. Golovchenko, Doppler Broadening of In-Flight Positron Annihilation Radiation due to Electron Momentum, Phys. Rev. Lett. 86 (2001) 5612-5615.

[12] J. Čížek, M. Vlček, I. Procházka, Digital spectrometer for coincidence measurement of Doppler broadening of positron annihilation radiation, Nucl. Instr. Meth. A 623 (2010) 982-994.

[13] M. Butterling, W. Anwand, G. Brauer, T.E. Cowan, A. Hartmann, M. Jungmann, K. Kosev, R. Krause-Rehberg, A. Krille, R. Schwengner, A. Wagner, Positron annihilation spectroscopy using high-energy positrons, Phys. Status Solidi A 207 (2010) 334–337.

[14] M. Butterling, W. Anwand, T.E. Cowan, A. Hartmann, M. Jungmann, R. Krause-Rehberg, A. Krille, A. Wagner, Gamma-induced Positron Spectroscopy (GiPS) at a superconducting electron linear accelerator, Nucl. Instr. Meth. B 269 (2011) 2623-2629.

[15] J. Čížek, M. Vlček, I. Procházka, Investigation of positron annihilation in flight using digital coincidence Doppler broadening spectrometer, New Journal of Physics (2012) in print.

Near-Surface Depth Profiling of Solids by Mono-Energetic Positrons
10.4028/www.scientific.net/DDF.331

Low Background Digital Coincidence Spectrometer – A Tool for Investigation of Positron Annihilation in Flight
10.4028/www.scientific.net/DDF.331.53